

Observing Health Outcomes Using Remote Sensing Imagery and Geo-Context Guided Visual Transformer

Yu Li, *Member, IEEE*, Guilherme N. DeSouza, *Senior Member, IEEE*, Praveen Rao, *Senior Member, IEEE*, Chi-Ren Shyu, *Senior Member, IEEE*

Abstract—Visual transformers have driven major progress in remote sensing image analysis, particularly in object detection and segmentation. Recent vision-language and multimodal models further extend these capabilities by incorporating auxiliary information, including captions, question and answer pairs, and metadata, which broadens applications beyond conventional computer vision tasks. However, these models are typically optimized for semantic alignment between visual and textual content rather than geospatial understanding, and therefore are not suited for representing or reasoning with structured geospatial layers. In this study, we propose a novel model that enhances remote sensing imagery processing with guidance from auxiliary geospatial information. Our approach introduces a geospatial embedding mechanism that transforms diverse geospatial data into embedding patches that are spatially aligned with image patches. To facilitate cross-modal interaction, we design a guided attention module that dynamically integrates multimodal information by computing attention weights based on correlations with auxiliary data, thereby directing the model toward the most relevant regions. In addition, the module assigns distinct roles to individual attention heads, allowing the model to capture complementary aspects of the guidance information and improving the interpretability of its predictions. Experimental results demonstrate that the proposed framework outperforms existing pretrained geospatial foundation models in predicting disease prevalence, highlighting its effectiveness in multimodal geospatial understanding.

Index Terms—remote sensing, visual transformer, guided attention, multimodal learning, geospatial data fusion, spatial context modeling

I. INTRODUCTION

WITH the increasing availability of high-resolution remote sensing images and advancements in deep neural networks, there has been a surge in studies focused on various detection and prediction tasks using remote

This paragraph of the first footnote will contain the date on which you submitted your paper for review, which is populated by IEEE.

Yu Li is with the Department of Electrical Engineering and Computer Science, University of Missouri, Columbia, MO 65201 USA (e-mail: ylrbc@missouri.edu).

Guilherme N. DeSouza is with the Department of Electrical Engineering and Computer Science, University of Missouri, Columbia, MO 65201 USA (e-mail: desouzag@missouri.edu).

Praveen Rao is with the Department of Electrical Engineering and Computer Science, University of Missouri, Columbia, MO 65201 USA (e-mail: praveen.rao@missouri.edu).

sensing images. These advancements have driven significant progress in tasks such as scene classification [1], [2], [3], object detection [4], [5], and land cover segmentation [6], [7], [8], contributing substantially to informed decision-making and policy development in fields like environmental management, urban planning, and agriculture. In most of these tasks, the goal of prediction or detection is typically confined to the input image itself. For instance, in scene classification and object detection, all the visual features necessary for the task are contained within the boundaries of the image. Similarly, land cover segmentation aims to partition the image into regions representing different types of land use or land cover based entirely on the spatial and spectral information present within the image. These tasks inherently focus on analyzing and interpreting the content of the input image without leveraging external data or contextual information.

As a result, most prior methods rely exclusively on the remote sensing image as input, with a primary focus on improving predictive performance. However, as methods have grown increasingly complex and incorporate specialized modules, explaining their prediction processes has become more challenging. While this lack of explainability may not pose significant concerns for some applications, it can be crucial in others where trust and transparency are essential, such as healthcare. In these scenarios, enhanced explainability can aid in better understanding model decisions, fostering trust, and ensuring ethical use of the technology.

One such application is the prediction of health outcomes for a specific region. Studies have shown that disparities in health outcomes can be attributed to a variety of factors, including socioeconomic conditions [9], [10], [11], environmental exposures [12], [13], [14], [15], and access to healthcare [16], [17], [18]. Interestingly, many of these factors can be indirectly captured and reflected in remote sensing images, such as through indicators of urban infrastructure

Chi-Ren Shyu is with the Department of Electrical Engineering and Computer Science, and the Institute for Data Science and Informatics, University of Missouri, Columbia, MO 65201 USA (e-mail: shyuc@missouri.edu).

The supplemental document provides detailed results for Section V-A-2 and examples for generated text summaries.

This work has been submitted to the IEEE for possible publication. Copyright may be transferred without notice, after which this version may no longer be accessible.

development [19], [20], vegetation cover [21], [22], [23], and air quality [24], [25]. Incorporating these spatial and environmental cues into health outcome prediction models presents an opportunity for more holistic analyses but also necessitates robust explainability to ensure that the insights derived are interpretable for public health interventions.

Tasks like predicting health outcomes can also benefit from additional information that is not contained within remote sensing images. For example, a local residential area shown in an image might have a higher incidence rate of certain diseases due to the presence of industries or sources of pollution located outside the boundaries of the image. Similarly, the prediction of prevalence for some diseases may require demographic information, such as the race or age distribution, which cannot be inferred solely from the image. These limitations highlight the need for integrating additional, potentially multimodal data sources, such as census data or environmental monitoring records, to improve prediction accuracy. However, the incorporation of such external data poses challenges for prior models, which are typically designed to operate on remote sensing imagery or in combination with textual data.

We propose a novel framework that addresses the limitations of prior approaches by integrating geospatial contextual layers into visual transformer architectures while enhancing the interpretability of model predictions. The main contributions of this work are as follows:

- 1) A guided attention module that incorporates contextual geospatial information into visual transformers, enabling the model to focus adaptively on task-relevant regions and features within remote sensing imagery.
- 2) A geospatial embedding mechanism that transforms heterogeneous geospatial data into spatially aligned embedding patches, facilitating effective multimodal representation learning.
- 3) An interpretable multimodal framework that bridges the gap between unimodal image-based models and real-world geospatial applications, providing improved transparency and explanatory power in prediction tasks, such as health outcome mapping.
- 4) A demonstrated practical impact, showing that the framework can reliably predict health outcomes by combining remote sensing imagery with only a small set of geospatial variables, reducing dependence on extensive and costly census data. The resulting attention maps further highlight spatial associations between environmental characteristics and specific disease categories, offering cues for subsequent studies in public health and urban management.

II. BACKGROUND

A. Vision Transformers with Remote Sensing Images

Since the introduction of the Vision Transformer (ViT) [26] for image classification, transformer-based architectures have become widely adopted across computer vision, including in remote sensing. Compared with natural images, remote sensing imagery presents unique challenges, such as top-down

perspective, large-scale spatial structures, and distinct object types and distributions. These differences motivate architectural adaptations tailored to this domain.

1) *Scene Classification*: Early studies demonstrated that ViT pretrained on natural images can perform competitively with CNNs for scene classification tasks in remote sensing [27]. Subsequent work explored training strategies to improve adaptation, including generative self-supervised learning [28], [29], multi-task learning [30], and contrastive learning frameworks such as ViT-CL [31]. Hybrid architectures combining CNNs and transformers have also been proposed, including dual-stream encoders (CTNet [32], L2RCF [33]), ResNet–Transformer fusion models (Resformer [34], TRS [35]), and multi-scale patch designs (LG-ViT [36]). Other efforts such as TSTNet [37] incorporated edge-enhanced branches to address noise and data scarcity.

Beyond training approaches, several methods introduced architectural modifications specific to remote sensing. HHTL [38] adjusted patch generation to improve color consistency; DSS-TRM [39] and SpectralFormer [40] tailored transformer designs to hyperspectral data; MITformer [41], EMTCAL [42], and Yang et al. [43] integrated convolutional operations or enhanced attention mechanisms to encode local structure and multi-scale features. Despite these innovations, relatively few studies have focused on modifying attention mechanisms to incorporate external or auxiliary modalities.

2) *Object detection*: Transformer-based object detection in remote sensing often employs hybrid CNN-transformers designs to capture both local detail and global spatial context. Methods such as TRD [44], GOCPK [45], and CI_DETR [46] use CNN-derived feature pyramid as transformer inputs. Architectures including LPSW [47], EIA-PVT [48], LAST-Net [49], and the model by Lu et al. [50] incorporate convolutional blocks within or alongside transformer layers to strengthen local feature extraction, which is critical for detecting small, densely clustered objects like vehicles.

Other work focused on improved learning strategies or attention designs. Zhang et al. [51] applied adversarial and self-supervised pretraining; Zheng et al. [52] introduced the Feature Pyramid Transformer (FPT) to propagate attention across feature scales; and Yuan and Wei [53] leveraged cross-attention between RGB and infrared channels to improve multi-spectrum detection accuracy. Overall, object detection methods highlight the need for architectures that combine transformers’ global reasoning with mechanisms that handle domain-specific spatial structure.

B. Multi-Modal Models with Remote Sensing Images

1) *Modality-Separate Encoder Models*: Large vision-language models (VLM) such as CLIP [54] and ERNIE-ViL [55] have motivated multimodal learning in remote sensing, particularly for image-text retrieval. Early systems paired transformer-based image and text encoders (e.g., ViT and Transformer in [56]; SIRS [57]) and performed alignment by comparing features extracted from each modality independently. MSCMAT [58] extended this paradigm by introducing a multiscale alignment strategy for refined image-

text feature matching. CLIP-based adaptations later became dominant: PERT-RaMa [59] applied parameter-efficient tuning, CUP [60] introduced token generation while freezing CLIP weights, and methods such as CLGSA [61] and PR-CLIP [62] added attention refinements to strengthen image-text alignment within the dual-encoder design.

Recent efforts scaled these approaches using large remote sensing datasets. RemoteCLIP [63] leveraged diverse detection, segmentation, and text-image datasets; GeoRSCLIP [64] and SkyScript [65] compiled multimillion image-text pairs for CLIP-style training; CLIP-MoA [66] modified CLIP with gating for multi-task learning; and EarthGPT [67] combined CNN and ViT image encoders with a Llama-based text model. Most of these models maintain dual-encoder CLIP-style pipelines, benefiting from natural language supervision but still bound by token limits and language-model constraints.

These constraints pose challenges for incorporating high-dimensional geospatial layers. CLIP’s typical token budgets (77 for CLIP; 512–1024 for extended variants [68], [69]) cannot accommodate hundreds of geospatial variables unless expanded into long natural-language descriptions that exceed encoder capacities. Moreover, text inputs in VLMs usually describe visible scene content, whereas many geospatial variables capture latent socioeconomic, infrastructural, or environmental attributes that are not directly observable in imagery. As a result, standard multimodal VLMs struggle to model the weak and indirect correspondence between remote sensing imagery and structured geospatial data, motivating alternative cross-modal integration mechanisms.

2) *Guided Attention for Cross-Modal Interaction*: Although many multimodal systems adopt separate processing streams for different modalities and perform cross-modal interaction only after feature extraction, some studies explore earlier integration by introducing guidance into the attention computation. Guided attention generally refers to attention mechanisms that condition visual feature weighting on auxiliary inputs rather than relying solely on image-derived self-attention. Prior to the prevalence of transformers, early work such as the GAIN [70] demonstrated that externally supervised attention can improve visual localization by steering attention toward semantically relevant regions. Text-conditioned variants later enabled language-guided visual attention for tasks such as image captioning [71], and class-supervised attention mechanisms improved robustness in image classification by training attention maps to emphasize objects of specific categories [72]. Recent multimodal systems extend this concept by injecting textual, relational, or structural cues directly into attention modules, enabling cross-modal alignment for tasks in vision-language modeling and chart or document understanding [73], [74], [75].

In remote sensing, guided attention has been applied to incorporate auxiliary information such as segmentation masks for visual question answering [76], category-aware cues for semantic segmentation [77], and structural guidance for generative modeling [78]. These approaches demonstrate that conditioning attention on non-image sources can improve

robustness and support more accurate spatial localization. However, existing guided attention methods primarily leverage discrete or low-dimensional forms of guidance (e.g., masks, labels, or categorical priors) and are not designed to handle high-dimensional, continuous geospatial layers. As a result, current techniques remain limited in their ability to utilize rich geospatial context, underscoring the need for attention mechanisms that can incorporate structured geospatial information.

C. Health Outcome Prediction with Remote Sensing Images

Compared with traditional remote sensing tasks, predicting health outcomes from imagery remains limited. Most prior work extracts intermediate features and factors rather than training end-to-end predictors. Remote sensing images have been employed to estimate health-relevant environmental factors such as fire plumes [79], water tanks [80], livestock distribution [81], heavy metal concentrations [82], [83], and measures of environmental deprivation [84], [85]. Extracted features have then been linked to health outcomes through downstream models, such as obesity prediction using VGG features [86], cancer prevalence prediction using ResNet features [87], and COVID-19 risk factor prediction with AlexNet and XGBoost [88]. Other studies, such as [89], employed clustering of extracted image features to analyze associations with urban health indicators.

Only a small number of works perform direct end-to-end prediction of health outcomes. Levy et al. [90] used transfer learning with a pretrained ResNet to predict mortality rates from imagery sampled around schools, illustrating the feasibility of direct prediction but leaving the design of multimodal health-focused models largely unexplored.

Despite the rapid progress of transformer-based architectures in remote sensing reviewed in Sections II, existing models primarily focus on visual information extracted from imagery alone, often overlooking the rich geospatial context that governs many real-world phenomena. While recent variants of visual transformers have incorporated architectural enhancements, these efforts remain constrained to visual features and lack explicit mechanisms for integrating external geospatial data. Similarly, multimodal approaches inspired by vision-language models like CLIP have shown promise in aligning heterogeneous modalities, but their reliance on text encoders and fixed token capacities limits their applicability to high-dimensional geospatial layers. Moreover, such models are typically optimized for tasks with direct visual-semantic correspondence, whereas geospatial variables often represent latent environmental, socioeconomic, or infrastructural conditions that are not visually explicit. This gap is particularly critical in emerging applications such as health outcome prediction, where spatially distributed factors influence observable imagery in complex and indirect ways.

Therefore, there is a pressing need for a framework capable of jointly modeling remote sensing imagery and auxiliary geospatial layers through a unified representation that enables spatially aligned cross-modal reasoning and enhances interpretability in domain-informed downstream analyses.

> REPLACE THIS LINE WITH YOUR MANUSCRIPT ID NUMBER (DOUBLE-CLICK HERE TO EDIT) <

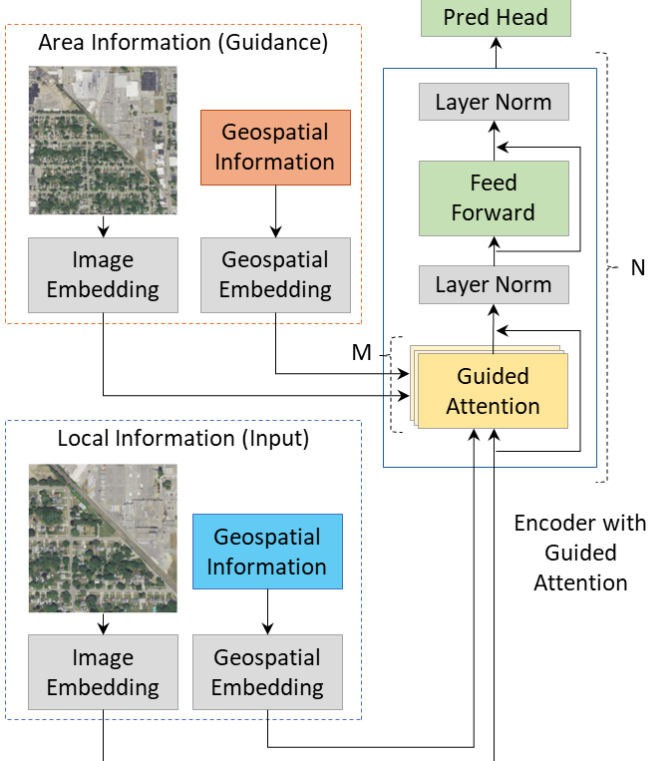


Fig. 1. Overall architecture of a variant of the proposed Geo-Context Guided Visual Transformer. Geospatial information is processed into Geospatial Embeddings and integrated with the image embedding in the proposed Guided Attention. Guidance information regulates the input processing through the generation of head and attention weights. The encoded features are subsequently passed to a prediction head to produce the final health outcome prediction.

III. METHODS

In this section, we present an interpretable framework with the Geo-Context Guided Visual Transformer (GCGVT) to effectively incorporate multimodal contextual information to enable health outcome prediction using remote sensing imagery.

A. Overview

We propose two variants of GCGVT that integrate multimodal contextual information and enhance interpretability, each motivated by a distinct design hypothesis presented in Section III-D. Fig. 1 presents the architecture of the first variant, which incorporates area-level contextual guidance in conjunction with local data. Geospatial information is first processed into spatially aligned geospatial embeddings and then integrated with the embedded image through the Guided Attention (GA) module. As shown in Fig. 1, the model combines these multimodal features through GA to produce a unified representation, which is subsequently passed to a prediction head for health outcome estimation. At the core of both architectures is the GA (Fig. 2), a novel mechanism that incorporates auxiliary guidance to modulate attention weights

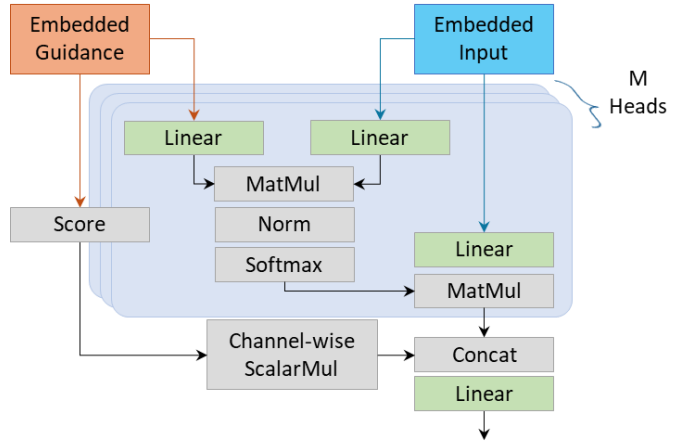


Fig. 2. Architecture of the Guided Attention module, showing how auxiliary guidance information is integrated with input embeddings. The embedded guidance (orange) is linearly projected and used to generate a modulation score through a sigmoid function, while the embedded input (blue) undergoes standard attention operations. The guidance score adjusts the attention output via channel-wise scaling before concatenation and linear transformation, producing the fused multimodal representation.

during input processing. By leveraging the GA, the model effectively utilizes multimodal data while maintaining the primary input as the main focus. Additionally, the architecture enforces distinct attention heads to specialize in different aspects of the guidance information, thereby improving the explainability of the resulting predictions.

B. Guided Attention

The GA builds upon conventional attention mechanisms, which prioritize different parts of the input based on their relevance to the task. Here, we extend the standard multi-head self-attention used in transformers by incorporating auxiliary information external to the input that serves as guidance for computing both attention weights and head-specific modulation. Unlike prior mechanisms, this approach preserves the primary input as the main focus of computation and introduces guidance-derived modulation of attention heads to improve the transparency of the attention process. As illustrated in Fig. 2, the proposed module leverages guidance information as a reference when generating attention weights, enhancing relevant image regions or features without fusing the guidance directly into the input. This explicit separation between guidance and input facilitates the modeling of their interactions and supports interpretable predictions by revealing how guidance influences attention and the input.

In addition to generating attention weights, the module introduces head weights to modulate the contribution of each attention head. These head weights are also derived from the guidance information, reinforcing the assignment of each head to a specific aspect of that information. Unlike traditional attention mechanisms, this approach offers greater interpretability by revealing the relative importance of different aspects of the guidance data and their corresponding attention

heads. The proposed module establishes a more transparent pathway from input to prediction: First, the head weights reflect the significance of each guidance aspect, while the interaction between attention weights and guidance provides insight into how various regions of the input contribute to the final prediction.

We denote the guidance information as X_G and the input as X_I . Following the conventional notation of self-attention, where K , Q , and V represent the key query and value matrices, respectively, we define:

$$K = W^K X_I, \quad Q = W^Q X_G, \quad V = W^V X_I, \quad (1)$$

where W^K , W^Q , and W^V are the corresponding weight matrices of key, query, and value transformations. The attention matrix A is calculated following the self-attention in a Transformer, but is further scaled by a scalar before concatenation:

$$A_i = h_i \cdot \text{softmax} \left(\frac{Q W_i^Q (K W_i^K)^T}{\sqrt{d_K}} \right) V W_i^V, \quad (2)$$

where A_i is the calculated attention weight for the attention head i ; W_i^K , W_i^Q , and W_i^V are the weight matrices for K , Q , and V ; and h_i is the scalar for A_i , which is the i^{th} element in the scalar vector H for attention heads:

$$H = \text{sigmoid}(\text{score}(X_G)) \quad (3)$$

The scalar vector H serves as a weight for each attention matrix across the heads and has dimensionality equal to the number of heads in the encoder. The score computation within GA is adaptable to the requirements of specific applications, allowing for the use of predefined formulas or the enforcement of desired semantic structures. This flexibility enables the model to scale the contribution of each attention head according to predefined categories or task-specific criteria. By examining the resulting attention weights, we can investigate how different regions of the input relate to the guidance information. Moreover, the guidance vector provides interpretive insight into which relationships are most influential for the task, thereby enhancing the model's transparency and explainability.

In our implementation, we replaced the scoring function with a two-layer fully connected neural network, as no well-established formula exists for our specific application. This learnable network allows the model to optimize the scoring function during training. To enhance explainability, we used only geospatial information to generate the weights for the attention heads. Each category within the geospatial data was processed independently to compute the corresponding weight for a specific attention head. Furthermore, to reinforce a clear correspondence between categories and attention heads, each geospatial category was assigned exclusively to one head. This design choice supports interpretability by enabling a direct mapping between semantic categories and attention mechanisms. Further implementation details are provided in the following section.

C. Geospatial Embedding

A key component of the proposed method is the integration of geospatial information through the Geospatial Embedding

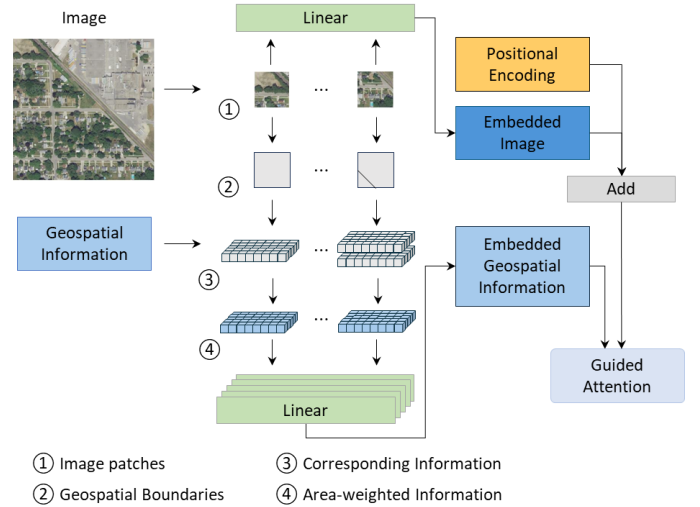


Fig. 3. Generation and integration of Geospatial Embeddings. Geospatial information is area-weighted based on image patch boundaries and processed through category-specific linear projections to produce embedded geospatial features, which are then combined with image embeddings and positional encodings.

(Fig. 3). By incorporating an additional modality, the network gains access to contextual information that may not be present in the image itself. This geospatial information also plays a critical role in the GA by helping the model differentiate between input data and guidance signals.

As shown in Fig. 3, geospatial data is extracted based on the spatial boundaries defined by the image patches, ensuring a natural spatial correspondence between the geospatial information and visual content. The value for each variable is calculated as the area-weighted average within this boundary. Each category of geospatial data is maintained as a separate channel throughout both preprocessing and computation. This categorical separation ensures that each category contributes only to its designated attention head.

Enforcing a one-to-one mapping between geospatial categories and attention heads enables interpretable attention dynamics, as each head reflects the influence of a specific geospatial factor. This structured design supports explainability by allowing model predictions to be interpreted in terms of the distinct relationships between visual features and geospatial context.

The geospatial embedding is processed in parallel with the image data as it is divided into patches. For each image patch, the corresponding geospatial boundary is overlaid at a specified resolution, and the associated geospatial information is extracted for each segment defined by that boundary. This information may include task-relevant contextual factors such as socio-economic status, education levels, environmental conditions, and other spatially distributed attributes.

For each segment i within a patch, a geospatial factor f_i is weighted by the segment's area $area_i$ of the segment relative to the image patch (Fig. 3). The aggregated value of a given geospatial factor f for the entire patch is computed as an area-weighted sum across all segments:

> REPLACE THIS LINE WITH YOUR MANUSCRIPT ID NUMBER (DOUBLE-CLICK HERE TO EDIT) <

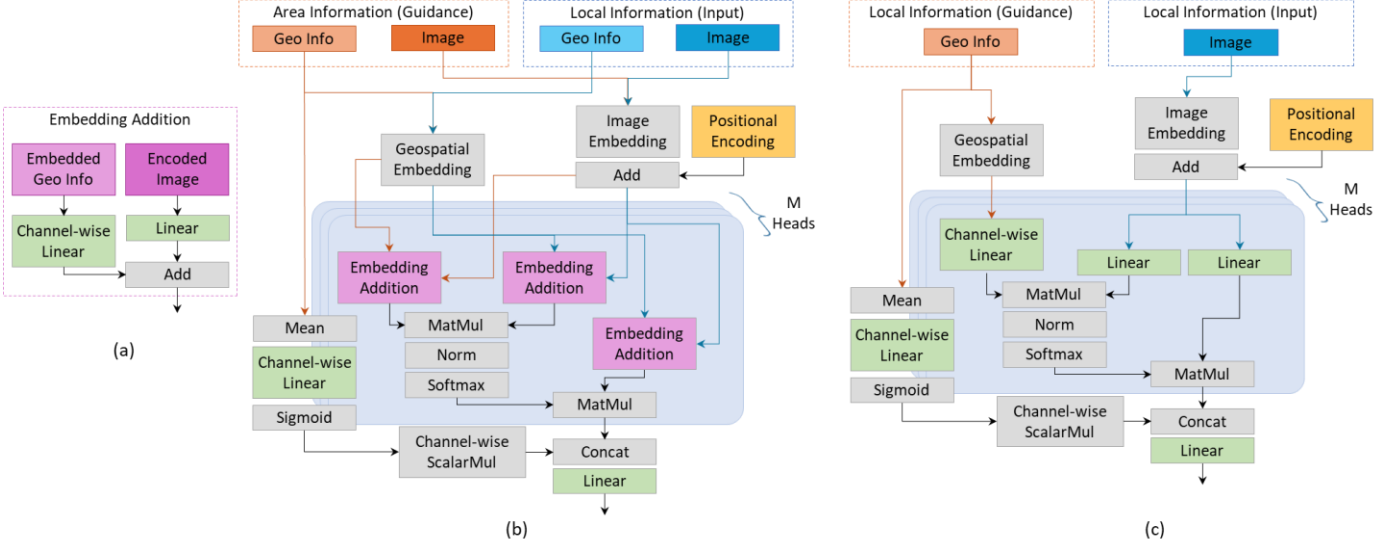


Fig. 4. Detailed architectures of the Geo-Context Guided Visual Transformer models: GCGVT-A (b) and GCGVT-G (c), both based on the proposed Guided Attention module. GCGVT-A incorporates local image and geospatial information as input, using the surrounding area as guidance, whereas GCGVT-G integrates image features with geospatial information to analyze how spatial context influences image-based representations.

$$f = \frac{\sum_i area_i * f_i}{\sum_i area_i} \quad (4)$$

Each category of geospatial information is then linearly projected to match the dimensionality of its corresponding attention head. The resulting geospatial embedding is subsequently fed into the GA alongside the encoded image features, as illustrated in Fig. 3.

D. Geo-Context Guided Visual Transformer Architectures

The overall architecture of the proposed GCGVT extends transformer-based visual models by replacing the conventional multi-head self-attention mechanism with the proposed GA. This design enables the model to jointly process both the remote sensing imagery and geospatial contextual information through guided multimodal interactions. Based on two complementary hypotheses, we develop two variants of the GCGVT to explore different roles of contextual guidance in multimodal representation learning.

The first variant, GCGVT-Area (GCGVT-A), is motivated by a public health hypothesis that environmental conditions in the broader surroundings may influence local health outcomes. For example, two visually similar residential areas exhibit different respiratory health risks if one is located near industrial zones or along the pathways of wildfire smoke. In this architecture (Fig. 4 (b)), the input consists of a high-resolution local RGB image and its corresponding geospatial layers that capture fine-grained structural and environmental attributes. The guidance is derived from a wider, zoomed-out context that encompasses both imagery and geospatial data, providing broader environmental cues. Through Geospatial Embedding and GA, the model integrates these complementary sources, enabling reasoning about the interactions between local features and regional contextual factors.

The second variant, GCGVT-Geo (GCGVT-G), is inspired by the previously discussed Guided Visual Search theory,

which posits that visual processing is influenced by prior knowledge and contextual cues. The underlying hypothesis is that the identical physical environments may be interpreted differently depending on socio-demographic attributes such as household composition or tenancy status. This reasoning parallels how human analysts interpret remote sensing imagery in light of background information. In this architecture (Fig. 4 (c)), the input is the local remote sensing image, while the guidance is derived from the geospatial embedding of the same spatial region. This configuration represents image interpretation under domain-specific contextual influence. Compared with GCGVT-A, GCGVT-G uses less external context and may therefore yield lower predictive performance. However, its explicit separation between image features (as input) and geospatial contextual information (as guidance) enhances interpretability by clarifying the contribution of each geospatial category.

For both variants, the models are implemented using a ViT backbone to isolate the effects of the proposed GA. Nevertheless, the overall architecture is modular and can be adapted to alternative visual transformer backbones, ensuring flexibility for future extensions and broader multimodal applications.

IV. EXPERIMENTS

To contextualize our experiments, we briefly restate the task setting in this work. Our objective is to evaluate models on problems in which remote sensing imagery alone may not capture all relevant factors, and where auxiliary geospatial information can provide complementary context. These tasks that are common in public health and environmental applications often involve influences that lie outside the spatial extent or visible content of the image. GA is therefore used to incorporate contextual geospatial layers when the visual input does not fully encode the predictive signal. The following

subsections describe the datasets, experimental configurations, and baselines used to assess this capability.

A. Dataset

Existing public datasets and benchmarks predominantly address standard computer vision tasks, such as image classification, semantic segmentation, and object detection. These tasks typically rely on input images that encapsulate all necessary information, rendering them unsuitable for the specific challenges identified in our study. Furthermore, while these datasets are often organized by category or object type, they generally omit geospatial information. To evaluate our model, we developed a dataset that integrates remote sensing as the primary input, augmented with corresponding geospatial information. Health outcomes were chosen as the prediction target, as they can be influenced directly by local features captured in the primary input and indirectly by broader contextual factors in the surrounding area or relevant geospatial information. This dataset fills a gap in the field as a task that can benefit from information outside of image and a benchmark for multimodal models.

1) Health Outcomes: Health outcomes were selected as the target variables for prediction, given their potential to benefit from additional contextual information. We utilized the PLACES dataset [91] from the Centers for Disease Control and Prevention, which offers comprehensive nationwide coverage and high spatial resolution at the census tract level. This dataset provides detailed measurements across various public health dimensions, including health outcomes, prevention efforts, health risk behaviors, disabilities, health status, health-related social needs, and social determinants of health. However, some factors could be directly inferred from economic status or were self-reported by individuals. To ensure reliability, our experiments focused exclusively on health outcomes derived from professional medical evaluations and excluded factors directly reflecting socioeconomic status. Specifically, among 12 total health outcomes, we selected the prevalence of arthritis, cancer, chronic obstructive pulmonary disease, coronary heart disease, depression, diabetes, chronic kidney disease, obesity, and stroke. Current asthma, high cholesterol among screened adults, and all teeth lost among adults older than 65 years were excluded since they could be directly correlated with environmental, socioeconomic, or demographic factors. Data from the year 2020 were used to minimize the impact of the COVID-19 pandemic while preserving the availability of high-resolution imagery. The prevalence values represent model-estimated percentages for each condition within each census tract, ranging from 0 to 100. Since a single sampled image might encompass multiple census tracts, we calculated the area-weighted average for each health outcome to serve as the ground truth for the corresponding sampled image.

2) Remote Sensing Images: To minimize the inclusion of unpopulated areas or regions lacking sufficient variation, we used historical redlining zones as a baseline for generating geospatial sampling points. Originally created in the 1930s to guide mortgage lenders, redlining zones categorized residential areas in major U.S. cities based on investment risk. Despite

their prohibition decades ago, these zones continue to influence various aspects of residents' lives [92], making them a suitable baseline for sampling images and corresponding health outcomes.

We obtained digitized redlining zone polygons from the Mapping Inequality dataset [93]. This dataset includes redlining designations at four risk levels across 138 cities in 44 U.S. states. By matching these geospatial locations with the PLACES dataset, we identified 14,330 valid areas. The centroid of each area was used as the sampling point for remote sensing images, ensuring minimal overlap between images from adjacent areas.

The remote sensing images were sourced from the National Agriculture Imagery Program (NAIP), which provides high spatial resolution imagery collected during the growing season to ensure consistency across states. Using the centroids of the redlining areas, we sampled images from the year closest to 2020. For each point, two image sizes were generated: local images (640×640 pixels) and area images (1280×1280 pixels). At a resolution of 60 cm/pixel, these images covered approximately 0.15 and 0.59 square kilometers, respectively. The area images were resized to 640×640 pixels using the bicubic interpolation method.

3) Geospatial Layers: For geospatial embeddings, we utilized the 2020 American Community Survey (ACS) data [94] provided by the United States Census Bureau. To achieve a balance between high-level insights and sufficient detail, we used the 5-year data profiles, which aggregate geospatial information over a five-year period ending in 2020. The dataset encompasses social, economic, housing, and demographic information for every census tract in the U.S., totaling more than 2,400 layers. However, certain categories were either overly detailed, such as specific construction years of houses or mortgage amounts, or had direct ties to health outcomes like disability rates and health insurance coverage. Such features were excluded to avoid having proxy of the health outcomes.

We selected ten broad categories from the dataset: age and sex, ancestry, education, employment, household, housing, income, origin, race, and residency, resulting in 228 variables. To account for the varying population distributions across states, percentage values were used to normalize the data. These percentages, ranging from 0 to 100, represent the proportion of the population meeting the criteria for each variable. For each image patch, the values were calculated as area-weighted averages derived from all census tracts overlapping with the patch as described in Geospatial Embedding in Methods.

B. Experiment Configuration

To evaluate the effectiveness of GCGVT and to characterize the role of each data modality, we designed our experiments around three complementary objectives. First, we assessed the overall multimodal performance of GCGVT when jointly incorporating imagery and geospatial information, enabling direct comparison with remote-sensing visual-language foundation models. Second, we examined the influence of geospatial data in isolation and in combination with imagery, motivated by the need to understand how effectively GCGVT

> REPLACE THIS LINE WITH YOUR MANUSCRIPT ID NUMBER (DOUBLE-CLICK HERE TO EDIT) <

leverages auxiliary geospatial layers and how performance changes when such information is limited or partially available. Third, we evaluated the model in an image-only setting to analyze how the GA leverages local and area imagery, and to benchmark against transformer-based architectures and pretrained remote sensing models. This structure ensures that each experiment isolates a specific aspect of the method, providing a comprehensive assessment of its capabilities.

As described in Section III-D, all variants of GCGVT used a ViT-base-16 backbone. Given the size of the available dataset, we configured the models with four encoder blocks and set the embedding and MLP dimensions to 1280 and 128, respectively. The class token was removed and replaced with average pooling to facilitate analysis of patch-level interactions. Due to architectural modifications, GCGVT-A and GCGVT-G were initialized with random weights and pretrained on MLRSNet [95] using an image classification task to learn general remote-sensing representations. All datasets were randomly divided using an 8:1:1 train, validation, test split, and models were pretrained and trained for 128 epochs.

For the multimodal evaluation, we compared GCGVT with several representative models designed for joint image-text understanding: CLIP [54], RemoteCLIP (RCLIP) [63], GeoRSCLIP (GeoRS) [64], and SkyCLIP (Sky) [65]. CLIP employed a ViT-base-16 backbone for direct comparison, while the three remote-sensing-specific models used ViT-large-14 due to the lack of publicly available base-sized variants. Because CLIP and related vision-language models require textual inputs to represent non-visual information, we implemented two geospatial encoding strategies. The first strategy (denoted txt, example available in Supplemental Document) converted all geospatial variables and their definitions into a natural-language summary generated using the Mistral model [96]. The second strategy (denoted int) represented the same variables as a space-separated sequence of integer values. These encodings allowed CLIP-based architectures to incorporate structured geospatial data within their predefined text-token constraints. These models were initialized using their publicly released pretrained weights,

typically derived from ImageNet or large-scale remote sensing datasets. CLIP’s image encoder was additionally fine-tuned on MLRSNet, as it was not originally optimized for remote sensing. This evaluation provides a broad comparison of multimodal fusion strategies, contrasting GCGVT’s guidance-based mechanism with text-aligned embeddings used in vision-language models.

To understand the contribution of geospatial information and the fusion mechanism, we conducted experiments focusing on GCGVT-A under settings where only geospatial embeddings or both were available. This analysis was motivated by the strong predictive capacity often seen in geospatial datasets and the need to examine how effectively GCGVT can leverage such information when the imagery is less informative or when geospatial variables are limited. By comparing performance across these configurations, we assess both the standalone value of geospatial layers and the added benefit of GCGVT’s spatially aligned fusion strategy.

Finally, to evaluate image-only performance and analyze the benefit of integrating multi-resolution visual information, we compared GCGVT-A and its local-only counterpart, GCGVT-Local (GCGVT-L), under conditions where the head weights were disabled. GCGVT-A maintained its input configuration that used local image as input and the area image as guidance, whereas GCGVT-L used the local image for both roles. We benchmarked these models against ViT-base-16 [26], Swin-v2-base [97], BEiT-base [98], PVT-v2-base [99], and the four multimodal baselines. Like GCGVT-A and GCGVT-L, these four vision-only models were initialized with random weights and pretrained on MLRSNet for fair comparison. This experiment isolates the contribution of area-level context and evaluates whether GCGVT’s architecture can more effectively exploit multi-resolution imagery than standard transformer-based approaches.

V. RESULTS

A. Performance Comparison and Analysis

Our experiments evaluated the ability of the proposed

TABLE I
OVERALL PERFORMANCE FOR EACH HEALTH OUTCOME WITH MULTI-MODAL MODELS

	GCGVT-A	GCGVT-G	CLIP-txt	CLIP-int	RCLIP-txt	RCLIP-int	GeoRS-txt	GeoRS-int	Sky-txt	Sky-int
Arthritis	0.84 [†]	0.79 [‡]	0.33	0.52	0.39	0.49	0.36	0.48	0.30	0.53
Cancer	0.86 [†]	0.85 [‡]	0.19	0.43	0.20	0.50	0.27	0.44	0.25	0.53
CHD	0.80 [†]	0.78 [‡]	0.22	0.39	0.27	0.41	0.22	0.38	0.25	0.40
COPD	0.83 [†]	0.81 [‡]	0.36	0.50	0.38	0.54	0.36	0.51	0.34	0.53
Depression	0.85 [†]	0.83 [‡]	0.34	0.40	0.42	0.49	0.45	0.49	0.43	0.48
Diabetes	0.88 [†]	0.88 [‡]	0.31	0.61	0.35	0.53	0.37	0.57	0.35	0.63
Kidney	0.84 [†]	0.82 [‡]	0.20	0.47	0.29	0.51	0.26	0.49	0.23	0.50
Obesity	0.90 [†]	0.89 [‡]	0.47	0.66	0.47	0.63	0.45	0.61	0.50	0.64
Stroke	0.85 [†]	0.84 [‡]	0.25	0.59	0.29	0.59	0.35	0.57	0.39	0.55
Mean	0.85 [†] ±0.03	0.83 [‡] ±0.04	0.30±0.09	0.51±0.09	0.34±0.08	0.52±0.06	0.34±0.08	0.50±0.07	0.34±0.08	0.53±0.07

Note: [†] and [‡] indicates the best and second-best performance, respectively, for the outcome. Row Mean shows the mean plus-minus standard deviation across all health outcomes.

> REPLACE THIS LINE WITH YOUR MANUSCRIPT ID NUMBER (DOUBLE-CLICK HERE TO EDIT) <

TABLE II
MEAN PERFORMANCE OF GCGVT-A WITH LIMITED
GEOSPATIAL INFORMATION

Category	Image & Geo	Geo Only	Diff
Age	0.64±0.09	0.36±0.17	0.28±0.13
Ancestry	0.60±0.12	0.39±0.12	0.21±0.06
Education	0.61±0.09	0.44±0.13	0.17±0.11
Employment	0.69±0.06	0.51±0.16	0.19±0.13
Household	0.68±0.05	0.53±0.12	0.16±0.12
Housing	0.70±0.05	0.63±0.10	0.07±0.10
Income	0.75±0.04	0.66±0.13	0.09±0.11
Origin	0.48±0.12	0.30±0.08	0.18±0.10
Race	0.60±0.13	0.42±0.16	0.18±0.13
Residency	0.46±0.10	0.09±0.08	0.41±0.12
All	0.85±0.03	0.83±0.04	0.02±0.03

Note: Column Image & Geo shows the mean plus-minus standard deviation across all health outcomes using both image and geospatial information, and Geo Only is using only geospatial embedding. Column Diff shows the mean plus-minus standard deviation of difference between Image & Geo and Geo Only across outcomes.

models to predict multiple health outcomes. These outcomes include various disease prevalence at the census tract level. To assess quantitative performance, we measured the coefficient of determination (R^2) between model predictions and ground-truth prevalence values. R^2 provides a normalized and outcome-independent measure of predictive accuracy, allowing comparison across variables with differing means and variances. The following subsections report results for the three experimental settings introduced previously, corresponding directly to the evaluation design described in Section IV-B.

1) *Overall Performance*: To assess multimodal predictive performance, we compared GCGVT-A and GCGVT-G with recent remote-sensing vision-language foundation models, using both imagery and geospatial variables (Table I). Because CLIP-based baselines require textual representations of

auxiliary variables, we evaluated two previously described encoding strategies (txt and int). This experiment addresses our first objective: establishing whether GA improves multimodal fusion relative to large-scale pretrained models.

As shown in Table I, the GCGVT-A achieved the highest overall performance and consistently outperformed other models across all disease outcomes, with GCGVT-G closely following. In contrast, the pretrained vision-language models generally exhibited performance scores approximately 0.3 lower than our proposed methods. This discrepancy is expected, as geospatial information in remote sensing tasks is not directly observable from images. While certain aspects, such as housing and income levels, may be inferred from surrounding structures, these relationships are implicit and complex.

Interestingly, for the vision-language models, encoding geospatial information as descriptive summaries proved less effective than using raw integer representations. This may be due to token limitations, which force summaries to be overly concise and potentially omit critical numerical relationships. By incorporating all geospatial variables as geospatial embeddings and leveraging them as guidance, our models effectively captured the relationships between geospatial information and image features, leading to superior accuracy.

2) *Ablation Study of Geospatial Information*: To isolate the contribution of structured geospatial data, we evaluated the GCGVT-A architecture using only geospatial embeddings as input. This setting examines how effectively the model leverages non-visual information and how performance degrades when imagery is removed. We further assessed the predictive value of each geospatial category individually. These evaluations correspond to our second objective of characterizing the standalone and partial utility of geospatial variables.

Table II shows the mean performance of GCGVT-A across all health outcomes with limited geospatial information. Detailed results for each outcome can be found in Supplemental Table I. As shown in Table II, with only all geospatial categories (row All), it can achieve comparable performance with all available input (image and geospatial information) with

TABLE III
IMAGE-ONLY PERFORMANCE COMPARISON

	GCGVT-A	GCGVT-L	CLIP	RCLIP	GeoRS	Sky	ViT	Swin-v2	BEiT	PVTv2
Arthritis	0.42 [†]	0.39 [†]	0.29	0.38	0.39 [‡]	0.36	0.25	0.39 [‡]	0.29	0.32
Cancer	0.26	0.19	0.26	0.32 [‡]	0.33 [†]	0.31	0.26	0.27	0.18	0.26
CHD	0.28 [‡]	0.26	0.25	0.27	0.18	0.29 [†]	0.18	0.24	0.22	0.21
COPD	0.44 [†]	0.39 [‡]	0.32	0.31	0.39 [‡]	0.34	0.30	0.31	0.19	0.31
Depression	0.61 [†]	0.58 [‡]	0.39	0.41	0.43	0.42	0.46	0.40	0.42	0.36
Diabetes	0.42 [‡]	0.39	0.34	0.41	0.44 [†]	0.40	0.20	0.28	0.24	0.27
Kidney	0.31 [†]	0.27	0.23	0.27	0.26	0.28 [‡]	0.15	0.16	0.12	0.15
Obesity	0.55 [‡]	0.51	0.49	0.55 [‡]	0.58 [†]	0.55 [‡]	0.32	0.40	0.37	0.40
Stroke	0.35	0.31	0.19	0.37 [†]	0.37 [†]	0.36 [†]	0.18	0.20	0.14	0.24
Mean	0.41±0.11 [†]	0.37±0.12 [‡]	0.31±0.09	0.37±0.08 [‡]	0.37±0.11 [‡]	0.37±0.08 [‡]	0.25±0.09	0.29±0.08	0.24±0.09	0.28±0.07

Note: [†] and [‡] marks the best and second-best performance, respectively, for the outcome. Row Mean shows the mean plus-minus standard deviation for the model.

> REPLACE THIS LINE WITH YOUR MANUSCRIPT ID NUMBER (DOUBLE-CLICK HERE TO EDIT) <

a mean performance difference of 0.02, showing strong correlation between various demographic and socioeconomic status and health outcomes.

However, we can also observe that using only one category, there is a significant drop in performance in almost all cases compared to having image as part of the input. Among the categories, economic status factors, including housing and income, were most correlated to various health outcomes. In general, adding remote sensing imagery to one category of geospatial information can help with prediction with a large margin with 0.07 to 0.41 mean performance differences, suggesting the effectiveness of the combination of remote sensing imagery with geospatial information. The table also revealed a difference between outcomes. Interestingly, no single category had comparable performance in depression as in other outcomes (Supplemental Table I), a result indicating that residential environment, something that can mainly be seen from visual features, played a more important role for depression prevalence prediction.

These results with limited geospatial information suggest that remote sensing imagery, when combined with select geospatial attributes, can achieve performance comparable to models that use all available categories. This finding demonstrates the potential to predict health outcomes even when certain geospatial data are missing, unreliable, or difficult to obtain, which is an important consideration as remote sensing imagery becomes increasingly accessible. We further evaluated two-category combinations alongside remote sensing imagery and compared them with the baseline that uses only all geospatial categories (G with All categories in Supplemental Table I). The top three performing combinations are reported in Supplemental Table II. Across all health outcomes, prediction was feasible with only two geospatial categories in addition to imagery, with performance declines of no more than 0.05. In some cases, such as AgeSex+Housing for arthritis and Income+Race for depression, the reduced-input models even outperformed the full geospatial model. These results highlight a practical advantage that accurate prediction is possible with substantially less geospatial information, thereby reducing costly data collection requirements.

3) Ablation Study of Remote Sensing Imagery: To quantify the benefit of incorporating area-level visual context, we also performed image-only experiments. In this setting, GCGVT-A used local imagery with area-level guidance, while GCGVT-L provided a controlled baseline using only local imagery. Benchmark transformer models received the area image as their sole input. This analysis addresses our third objective: determining the effectiveness of GCGVT's Guided Attention mechanism for multi-resolution visual information in the absence of geospatial data.

As shown in Table III, GCGVT-A consistently outperformed GCGVT-L across all outcomes, demonstrating that incorporating area-level guidance improves prediction. Moreover, GCGVT-A achieved higher overall performance than other models that also used area images as input, indicating that the guidance mechanism effectively integrates fine-grained

local details with broader contextual information. This ability to fuse information across resolutions enhances performance in typical computer vision tasks and highlights the value of using complementary images to capture complex geospatial relationships. The improved performance achieved by fusing local and area images demonstrates not only the benefit of incorporating related imagery at different spatial resolutions but also the potential to effectively integrate images with distinct yet intrinsically related visual features.

B. Prediction Visualization and Explanation

With the proposed GA, the generated attention weights on the input are structured in a way that facilitates interpretability. The head modulation mechanism provides a straightforward means of assessing the relative importance of different geospatial categories. Using this information, we can identify the attention maps of heads and tokens that contribute most to prediction. Importantly, the explicit separation of categories allows us to examine which image regions or features are most relevant to a given token within a specific geospatial category—an analysis not possible with conventional attention mechanisms. To complement this, we also visualized the SHAP values of both input and guidance for comparative interpretation.

1) Visualization of GCGVT-G: We first examined the explainability of GCGVT-G visualizations, as this variant employs separate pathways for image input and geospatial guidance. Attention maps were generated in two ways: (1) by identifying the most important head based on head weights and visualizing the tokens with the highest summed weights, and (2) by identifying the most important token in the guidance via head-averaged weights and visualizing both its averaged attention map and the most influential heads. These complementary approaches reveal different perspectives on geospatial-image interactions.

Fig. 5 presents representative examples of GCGVT-G visualizations. Each row corresponds to a specific input and health outcome. For reference, the numbers in parentheses indicate the learned head weights, which quantify the relative influence assigned to each geospatial category in GA. The first three rows show predictions of depression prevalence. The first example depicts a moderate-density residential area, where the most influential categories are origin (0.87) and employment (0.87). Their corresponding attention maps (columns C and D) highlight different spatial regions: origin guidance emphasizes the upper portion of the image while employment guidance concentrates on the top-left residential block. The associated token visualization (column K) suggests that this block may possess distinct employment-related characteristics strongly tied to depression prevalence. In contrast, the least influential category, age (0.0), yields attention maps with little meaningful correspondence to image structure.

The second and third rows show areas with greater vegetation and lower depression prevalence. In both, education (0.99, 0.77) and origin (0.50, 0.57) are most influential, yet the associated image features differ. For education, attention in row 2 centers on farmland rather than residential zones; while in row

> REPLACE THIS LINE WITH YOUR MANUSCRIPT ID NUMBER (DOUBLE-CLICK HERE TO EDIT) <

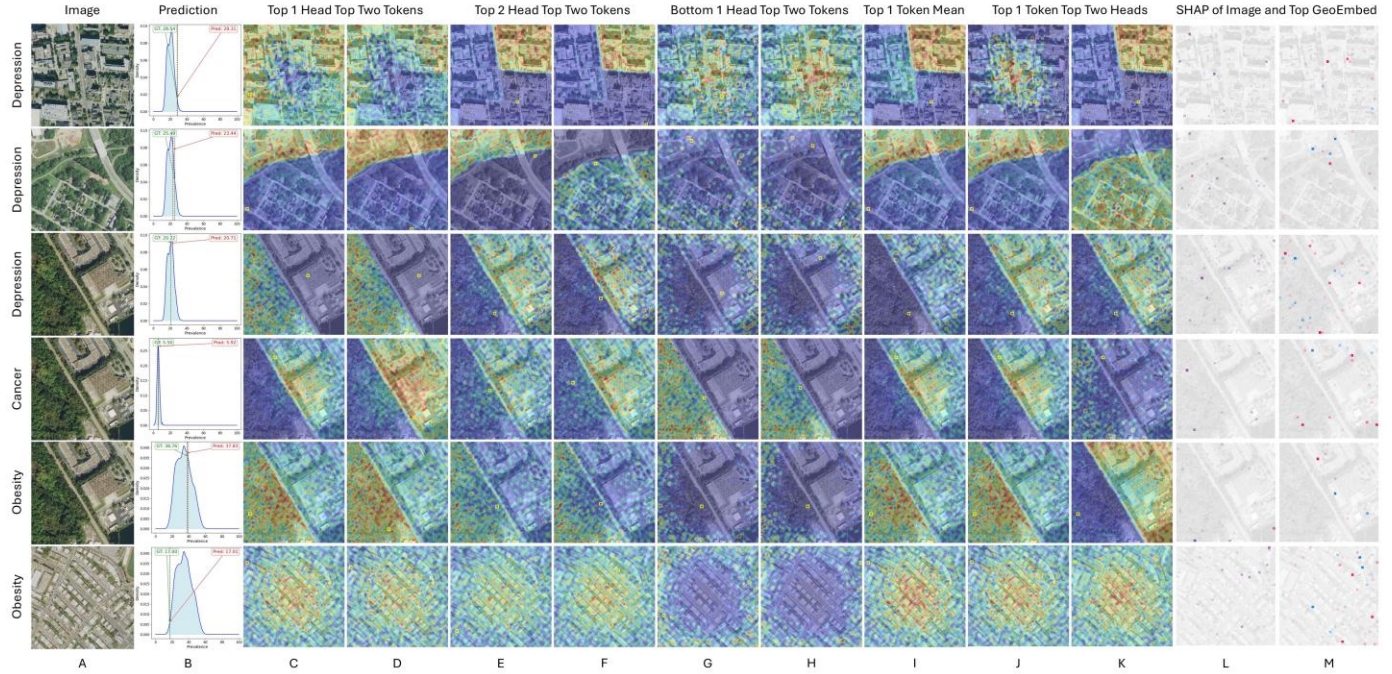


Fig. 5. Examples of attention map visualization of various outcomes by GCGVT-G. Each row represents one input sample. Column A shows the raw input image; Column B overlays the model prediction against ground truth on a kernel density estimate of all ground truth values. Columns C–D display the top two tokens from the category with highest head weight; Columns E–F from the second-highest category; and Columns G–H from the lowest-ranked category. Column I shows the most influential token averaged across heads, and columns J–K present the top two heads associated with this token. Columns L–M visualize SHAP value of input image and geospatial embedding of top category. Yellow squares in columns C to K are tokens of interest.

3 it highlights on a natural area adjacent to a residential complex. These findings suggest that educational attributes linked to non-residential land use may contribute to lower depression rates. For origin, row 2 emphasizes both farmland and low-density housing, while row 3 focuses more on the residential complex, potentially reflecting differences in population nativity between rural and urban areas.

Across these three depression examples, the model not only achieves high predictive accuracy but also reveals how specific geospatial factors shape the visual cues used in prediction. Because GA disentangles the influence of each geospatial category, the resulting maps show which spatial area correspond to which population characteristics, for example, how employment-related guidance consistently emphasizes built-environment structures such as housing blocks or road-access patterns. This category-specific linkage provides interpretability relevant for public health as it clarifies why an area's physical form may be associated with certain health outcomes and enables researchers to trace predictions back to distinct socioeconomic or demographic mechanisms. In contrast, SHAP visualizations (columns L–M) highlight important pixels but do not differentiate which population factors they relate to, whereas the GCGVT-G maps attribute salient image regions to semantically meaningful geospatial categories, offering a more interpretable cross-modal explanation.

The fourth and fifth rows of Fig. 5 illustrate cancer and obesity prevalence predictions using the same input as Example 3. In both cases, origin is the most important category (0.96,

0.97). However, the second category differs: household (0.55) for cancer and ancestry (0.46) for obesity. The spatial focus also varies by outcome: attention for cancer concentrates on the residential complex, whereas for obesity it shifts toward the adjacent natural area. This demonstrates the model's ability to provide outcome-specific interpretations by disentangling how geospatial guidance interacts with image features.

Finally, some less informative visualizations were observed. The last row of Fig. 5 shows a densely built residential area with little spatial variation. Attention maps across categories converge on central housing regions, producing limited explanatory value despite accurate prediction. This suggests that when image features lack meaningful heterogeneity, their alignment with geospatial guidance may be less interpretable.

2) *Visualization of GCGVT-A*: For GCGVT-A, both the input and the guidance consist of an image paired with geospatial embeddings. Consequently, the interactions occur between regions of the two inputs, particularly when a patch outside the local input area exerts distinct attention on the local area. Because the modalities are less clearly separated than in GCGVT-G, the resulting attention maps are generally less interpretable. Fig. 6 presents visualization examples of GCGVT-A, following the same layout as Fig. 5. The first and second rows correspond to the same regions and outcomes as the first and third rows of Fig. 5. Although the overall prediction accuracy is comparable, the attention patterns differ substantially. Unlike GCGVT-G, where attended regions are

> REPLACE THIS LINE WITH YOUR MANUSCRIPT ID NUMBER (DOUBLE-CLICK HERE TO EDIT) <

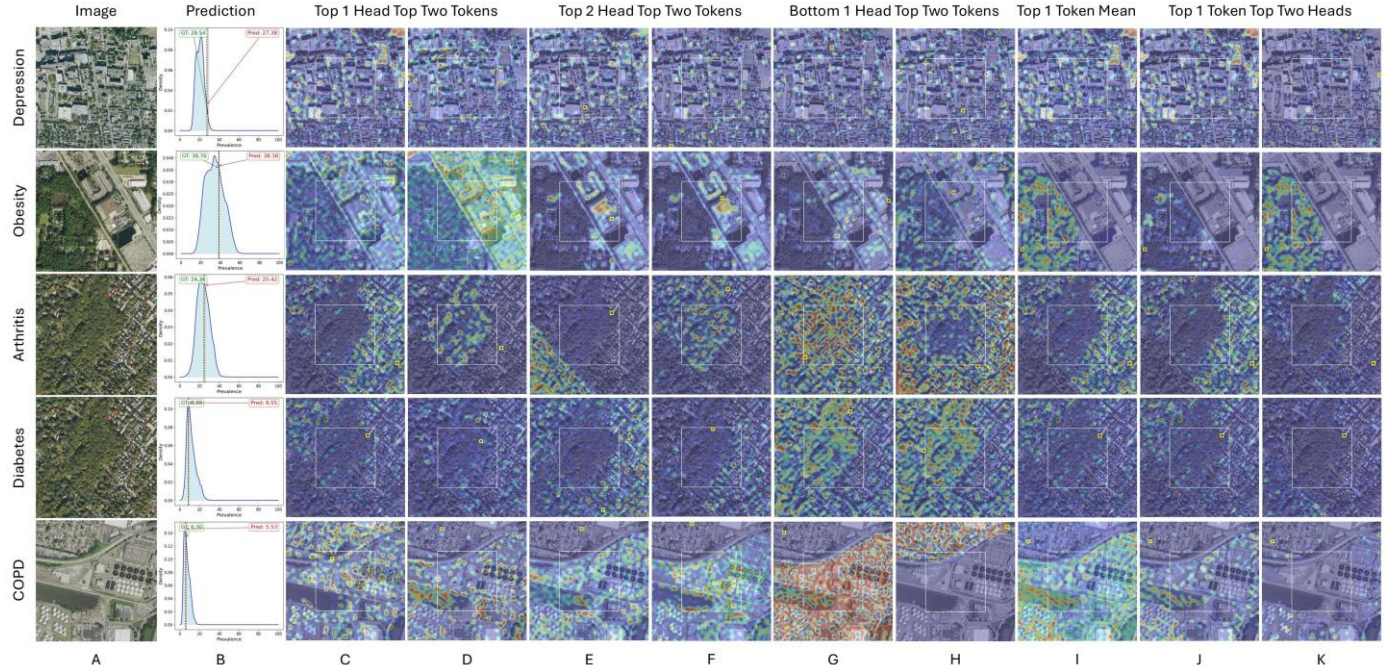


Fig. 6. Examples of attention map visualization of various outcomes by GCGVT-A. Similar to Figure 4, each row represents one input sample. Column A shows the raw input image; Column B overlays the model prediction against ground truth on a kernel density estimate of all ground truth values. Columns C–D display the top two tokens from the category with highest head weight; Columns E–F from the second-highest category; and Columns G–H from the lowest-ranked category. Column I shows the most influential token averaged across heads, and columns J–K present the top two heads associated with this token. Yellow squares in columns C to K are tokens of interest.

clearly delineated, GCGVT-A often produces more diffuse maps.

Region-specific interactions, however, remain evident in certain cases. In columns E and F of the second row, where the attention head corresponds to the housing category (0.94), attention is primarily focused on the apartment complex, indicating that the head has learned to capture visual features associated with housing structures. Another example appears in the last row, which predicts the prevalence of COPD with decent accuracy. The image depicts a residential area adjacent to an industrial zone, separated only by a road. Except for columns C and H, the top attention maps show that, when focusing on patches within the residential area, the prediction of lung-related disease benefits from attending to nearby industrial facilities.

Rows four and five of Fig. 6 illustrate predictions for arthritis and diabetes within the same region. Here, attention varies by outcome: predictions for arthritis highlight both residential and natural areas, whereas attention for diabetes appears less spatially structured. These variations indicate that the model learns distinct spatial features depending on the prediction target and local context.

Overall, GCGVT-A achieves superior predictive performance by leveraging broader regional context and richer multimodal information. However, its attention visualizations are generally less interpretable than those of GCGVT-G, as geospatial embeddings are integrated into both the input and guidance, complicating the separation of modality-specific contributions.

C. Summary

Across all evaluation tasks, GCGVT demonstrates an advantage over both vision-only baselines and geospatial vision-language foundation models. These results highlight the effectiveness of incorporating spatially aligned geospatial information through GA, enabling the model to leverage complementary cues that are not directly observable in remote sensing imagery. Between the two variants, GCGVT-A benefits from broader contextual embeddings and achieves the highest overall performance, whereas GCGVT-G provides more interpretable attention maps by restricting guidance to geospatial layers while using imagery as the sole primary input.

The models also exhibit strong practical efficiency: competitive performance can be achieved with only a small subset of geospatial variables, indicating that the framework remains effective in data-limited settings and may reduce dependence on comprehensive census-scale inputs. Beyond predictive accuracy, the category-specific attention patterns produced by both variants reveal distinct spatial associations between demographic or environmental factors and built-environment features, offering interpretable insights that complement quantitative results. These visual explanations provide clearer interpretability than traditional pixel-importance methods and support the generation of public-health-relevant spatial insights.

VI. CONCLUSION

This study introduced the Geo-Context Guided Visual Transformer, a multimodal framework that integrates geospatial information with remote sensing imagery through spatially aligned Geospatial Embeddings and a Guided Attention mechanism. By structuring auxiliary geospatial variables into region-level embeddings and using guidance to regulate attention, the framework enables localized interaction between modalities while preserving interpretable attention pathways.

Although the proposed approach demonstrates competitive performance and improved interpretability, several limitations remain. The current design assumes consistent spatial alignment between imagery and geospatial layers and may incur additional computational cost when incorporating high-dimensional auxiliary variables. Future work will explore scalable representations of geospatial context, extensions to temporal remote sensing, and broader applications across Earth observation tasks. Overall, GCGVT provides a flexible and interpretable foundation for geospatially informed multimodal modeling within transformer-based architectures.

ACKNOWLEDGMENT

The Mistral model [96] was used to create summaries of geospatial information for compared models with “-txt” suffix in Table I. Examples of generated summaries are available in Supplemental Table III.

REFERENCES

- [1] G. Cheng, J. Han, and X. Lu, “Remote Sensing Image Scene Classification: Benchmark and State of the Art,” *Proc. IEEE*, vol. 105, no. 10, pp. 1865–1883, 2017, doi: 10.1109/JPROC.2017.2675998.
- [2] G. Cheng, X. Xie, J. Han, L. Guo, and G.-S. Xia, “Remote Sensing Image Scene Classification Meets Deep Learning: Challenges, Methods, Benchmarks, and Opportunities,” *IEEE J. Sel. Top. Appl. Earth Obs. Remote Sens.*, vol. 13, pp. 3735–3756, 2020, doi: 10.1109/JSTARS.2020.3005403.
- [3] A. Thapa, T. Horanont, B. Neupane, and J. Aryal, “Deep Learning for Remote Sensing Image Scene Classification: A Review and Meta-Analysis,” *Remote Sens.*, vol. 15, no. 19, 2023, doi: 10.3390/rs15194804.
- [4] K. Li, G. Wan, G. Cheng, L. Meng, and J. Han, “Object Detection in Optical Remote Sensing Images: A Survey and a New Benchmark,” *ISPRS J. Photogramm. Remote Sens.*, vol. 159, pp. 296–307, 2020, doi: <https://doi.org/10.1016/j.isprsjprs.2019.11.023>.
- [5] S. Gui, S. Song, R. Qin, and Y. Tang, “Remote Sensing Object Detection in the Deep Learning Era—A Review,” *Remote Sens.*, vol. 16, no. 2, 2024, doi: 10.3390/rs16020327.
- [6] F. Mohammadimanesh, B. Salehi, M. Mahdianpari, E. Gill, and M. Molinier, “A New Fully Convolutional Neural Network for Semantic Segmentation of Polarimetric SAR Imagery in Complex Land Cover Ecosystem,” *ISPRS J. Photogramm. Remote Sens.*, vol. 151, pp. 223–236, 2019, doi: <https://doi.org/10.1016/j.isprsjprs.2019.03.015>.
- [7] C. Zhang *et al.*, “Joint Deep Learning for land cover and land use classification,” *Remote Sens. Environ.*, vol. 221, pp. 173–187, 2019, doi: <https://doi.org/10.1016/j.rse.2018.11.014>.
- [8] R. Li *et al.*, “Multiattention Network for Semantic Segmentation of Fine-Resolution Remote Sensing Images,” *IEEE Trans. Geosci. Remote Sens.*, vol. 60, pp. 1–13, 2022, doi: 10.1109/TGRS.2021.3093977.
- [9] B. Galobardes, J. Lynch, and G. D. Smith, “Measuring Socioeconomic Position in Health Research,” *Br. Med. Bull.*, vol. 81–82, no. 1, pp. 21–37, Feb. 2007, doi: 10.1093/bmb/ldm001.
- [10] P. Demakakos, J. Nazroo, E. Breeze, and M. Marmot, “Socioeconomic status and health: The role of subjective social status,” *Soc. Sci. Med.*, vol. 67, no. 2, pp. 330–340, 2008, doi: <https://doi.org/10.1016/j.socscimed.2008.03.038>.
- [11] S. Stringhini *et al.*, “Association of Socioeconomic Position With Health Behaviors and Mortality,” *JAMA*, vol. 303, no. 12, pp. 1159–1166, Mar. 2010, doi: 10.1001/jama.2010.297.
- [12] S. H. Swan, “Environmental Phthalate Exposure in Relation to Reproductive Outcomes and Other Health Endpoints in Humans,” *Environ. Res.*, vol. 108, no. 2, pp. 177–184, 2008, doi: <https://doi.org/10.1016/j.envres.2008.08.007>.
- [13] J. M. Braun *et al.*, “Cohort Profile: The Health Outcomes and Measures of the Environment (HOME) study,” *Int. J. Epidemiol.*, vol. 46, no. 1, pp. 24–24, Mar. 2016, doi: 10.1093/ije/dwy006.
- [14] C. E. Reid, M. Brauer, F. H. Johnston, M. Jerrett, J. R. Balmes, and C. T. Elliott, “Critical Review of Health Impacts of Wildfire Smoke Exposure,” *Environ. Health Perspect.*, vol. 124, no. 9, pp. 1334–1343, 2016, doi: 10.1289/ehp.1409277.
- [15] E. M. Sunderland, X. C. Hu, C. Dassuncao, A. K. Tokranov, C. C. Wagner, and J. G. Allen, “A review of the pathways of human exposure to poly- and perfluoroalkyl substances (PFASs) and present understanding of health effects,” *J. Expo. Sci. Environ. Epidemiol.*, vol. 29, no. 2, pp. 131–147, Mar. 2019, doi: 10.1038/s41370-018-0094-1.
- [16] S. T. Syed, B. S. Gerber, and L. K. Sharp, “Traveling Towards Disease: Transportation Barriers to Health Care Access,” *J. Community Health*, vol. 38, no. 5, pp. 976–993, Oct. 2013, doi: 10.1007/s10900-013-9681-1.
- [17] N. Douthit, S. Kiv, T. Dwolatzky, and S. Biswas, “Exposing Some Important Barriers to Health Care Access in the Rural USA,” *Public Health*, vol. 129, no. 6, pp. 611–620, 2015, doi: <https://doi.org/10.1016/j.puhe.2015.04.001>.
- [18] W. J. Hall *et al.*, “Implicit Racial/Ethnic Bias Among Health Care Professionals and Its Influence on Health Care Outcomes: A Systematic Review,” *Am. J. Public Health*, vol. 105, no. 12, pp. e60–e76, 2015, doi: 10.2105/AJPH.2015.302903.

> REPLACE THIS LINE WITH YOUR MANUSCRIPT ID NUMBER (DOUBLE-CLICK HERE TO EDIT) <

- [19] J. V. Henderson, A. Storeygard, and D. N. Weil, “Measuring Economic Growth from Outer Space,” *Am. Econ. Rev.*, vol. 102, no. 2, pp. 994–1028, Apr. 2012, doi: 10.1257/aer.102.2.994.
- [20] N. Jean, M. Burke, M. Xie, W. M. A. Davis, D. B. Lobell, and S. Ermon, “Combining Satellite Imagery and Machine Learning to Predict Poverty,” *Science*, vol. 353, no. 6301, pp. 790–794, 2016, doi: 10.1126/science.aaf7894.
- [21] A. Mizen *et al.*, “The Use of Enhanced Vegetation Index for Assessing Access to Different Types of Green Space in Epidemiological Studies,” *J. Expo. Sci. Environ. Epidemiol.*, vol. 34, no. 5, pp. 753–760, Sep. 2024, doi: 10.1038/s41370-024-00650-5.
- [22] S. Martinuzzi, O. M. Ramos-González, T. A. Muñoz-Erickson, D. H. Locke, A. E. Lugo, and V. C. Radeloff, “Vegetation Cover in Relation to Socioeconomic Factors in a Tropical City Assessed from Sub-Meter Resolution Imagery,” *Ecol. Appl.*, vol. 28, no. 3, pp. 681–693, 2018, doi: <https://doi.org/10.1002/eaap.1673>.
- [23] M. Kelly, S. D. Blanchard, E. Kersten, and K. Koy, “Terrestrial Remotely Sensed Imagery in Support of Public Health: New Avenues of Research Using Object-Based Image Analysis,” *Remote Sens.*, vol. 3, no. 11, pp. 2321–2345, 2011, doi: 10.3390/rs3112321.
- [24] A. Hyder, H. J. Lee, K. Ebisu, P. Koutrakis, K. Belanger, and M. L. Bell, “PM2.5 Exposure and Birth Outcomes: Use of Satellite- and Monitor-Based Data,” *Epidemiology*, vol. 25, no. 1, 2014, [Online]. Available: https://journals.lww.com/epidem/fulltext/2014/01000/p_m2_5_exposure_and_birth_outcomes_use_of.12.aspx
- [25] C. Zhou, J. Chen, and S. Wang, “Examining the Effects of Socioeconomic Development on Fine Particulate Matter (PM2.5) in China’s Cities Using Spatial Regression and the Geographical Detector Technique,” *Sci. Total Environ.*, vol. 619–620, pp. 436–445, 2018, doi: <https://doi.org/10.1016/j.scitotenv.2017.11.124>.
- [26] A. Dosovitskiy *et al.*, “An Image is Worth 16x16 Words: Transformers for Image Recognition at Scale,” *CorR*, vol. abs/2010.11929, 2020, [Online]. Available: <https://arxiv.org/abs/2010.11929>
- [27] Y. Bazi, L. Bashmal, M. M. A. Rahhal, R. A. Dayil, and N. A. Ajlan, “Vision Transformers for Remote Sensing Image Classification,” *Remote Sens.*, vol. 13, no. 3, 2021, doi: 10.3390/rs13030516.
- [28] X. Sun *et al.*, “RingMo: A Remote Sensing Foundation Model With Masked Image Modeling,” *IEEE Trans. Geosci. Remote Sens.*, vol. 61, pp. 1–22, 2023, doi: 10.1109/TGRS.2022.3194732.
- [29] Y. Lin, L. He, D. Zhong, Y. Song, L. Wei, and L. Xin, “A High Spatial Resolution Aerial Image Dataset and an Efficient Scene Classification Model,” *IEEE Trans. Geosci. Remote Sens.*, vol. 62, pp. 1–13, 2024, doi: 10.1109/TGRS.2024.3382159.
- [30] Q. Li, Y. Chen, X. He, and L. Huang, “Co-Training Transformer for Remote Sensing Image Classification, Segmentation, and Detection,” *IEEE Trans. Geosci. Remote Sens.*, vol. 62, pp. 1–18, 2024, doi: 10.1109/TGRS.2024.3354783.
- [31] M. Bi, M. Wang, Z. Li, and D. Hong, “Vision Transformer With Contrastive Learning for Remote Sensing Image Scene Classification,” *IEEE J. Sel. Top. Appl. Earth Obs. Remote Sens.*, vol. 16, pp. 738–749, 2023, doi: 10.1109/JSTARS.2022.3230835.
- [32] P. Deng, K. Xu, and H. Huang, “When CNNs Meet Vision Transformer: A Joint Framework for Remote Sensing Scene Classification,” *IEEE Geosci. Remote Sens. Lett.*, vol. 19, pp. 1–5, 2022, doi: 10.1109/LGRS.2021.3109061.
- [33] M. Zhao, Q. Meng, L. Zhang, X. Hu, and L. Bruzzone, “Local and Long-Range Collaborative Learning for Remote Sensing Scene Classification,” *IEEE Trans. Geosci. Remote Sens.*, vol. 61, pp. 1–15, 2023, doi: 10.1109/TGRS.2023.3265346.
- [34] M. Li, J. Ma, X. Tang, X. Han, C. Zhu, and L. Jiao, “Resformer: Bridging Residual Network and Transformer for Remote Sensing Scene Classification,” in *IGARSS 2022 - 2022 IEEE International Geoscience and Remote Sensing Symposium*, 2022, pp. 3147–3150. doi: 10.1109/IGARSS46834.2022.9883041.
- [35] J. Zhang, H. Zhao, and J. Li, “TRS: Transformers for Remote Sensing Scene Classification,” *Remote Sens.*, vol. 13, no. 20, 2021, doi: 10.3390/rs13204143.
- [36] T. Peng, J. Yi, and Y. Fang, “A Local–Global Interactive Vision Transformer for Aerial Scene Classification,” *IEEE Geosci. Remote Sens. Lett.*, vol. 20, pp. 1–5, 2023, doi: 10.1109/LGRS.2023.3266008.
- [37] S. Hao, B. Wu, K. Zhao, Y. Ye, and W. Wang, “Two-Stream Swin Transformer with Differentiable Sobel Operator for Remote Sensing Image Classification,” *Remote Sens.*, vol. 14, no. 6, 2022, doi: 10.3390/rs14061507.
- [38] J. Ma, M. Li, X. Tang, X. Zhang, F. Liu, and L. Jiao, “Homo–Heterogenous Transformer Learning Framework for RS Scene Classification,” *IEEE J. Sel. Top. Appl. Earth Obs. Remote Sens.*, vol. 15, pp. 2223–2239, 2022, doi: 10.1109/JSTARS.2022.3155665.
- [39] B. Liu, A. Yu, K. Gao, X. Tan, Y. Sun, and X. Yu, “DSS-TRM: Deep Spatial–Spectral Transformer for Hyperspectral Image Classification,” *Eur. J. Remote Sens.*, vol. 55, no. 1, pp. 103–114, Dec. 2022, doi: 10.1080/22797254.2021.2023910.
- [40] D. Hong *et al.*, “SpectralFormer: Rethinking Hyperspectral Image Classification With Transformers,” *IEEE Trans. Geosci. Remote Sens.*, vol. 60, pp. 1–15, 2022, doi: 10.1109/TGRS.2021.3130716.
- [41] Z. Sha and J. Li, “MITformer: A Multiinstance Vision Transformer for Remote Sensing Scene Classification,” *IEEE Geosci. Remote Sens. Lett.*, vol. 19, pp. 1–5, 2022, doi: 10.1109/LGRS.2022.3176499.
- [42] X. Tang, M. Li, J. Ma, X. Zhang, F. Liu, and L. Jiao, “EMTCAL: Efficient Multiscale Transformer and Cross-Level Attention Learning for Remote Sensing Scene Classification,” *IEEE Trans. Geosci. Remote Sens.*, vol. 60, pp. 1–15, 2022, doi: 10.1109/TGRS.2022.3194505.
- [43] Y. Yang *et al.*, “An Explainable Spatial–Frequency Multiscale Transformer for Remote Sensing Scene

> REPLACE THIS LINE WITH YOUR MANUSCRIPT ID NUMBER (DOUBLE-CLICK HERE TO EDIT) <

Classification,” *IEEE Trans. Geosci. Remote Sens.*, vol. 61, pp. 1–15, 2023, doi: 10.1109/TGRS.2023.3265361.

[44] Q. Li, Y. Chen, and Y. Zeng, “Transformer with Transfer CNN for Remote-Sensing-Image Object Detection,” *Remote Sens.*, vol. 14, no. 4, 2022, doi: 10.3390/rs14040984.

[45] N. Mo and R. Zhu, “A Novel Transformer-Based Object Detection Method With Geometric and Object Co-Occurrence Prior Knowledge for Remote Sensing Images,” *IEEE J. Sel. Top. Appl. Earth Obs. Remote Sens.*, vol. 18, pp. 2383–2400, 2025, doi: 10.1109/JSTARS.2024.3518753.

[46] Y. Han, W. Meng, and W. Tang, “Capsule-inferenced Object Detection for Remote Sensing Images,” *IEEE J. Sel. Top. Appl. Earth Obs. Remote Sens.*, vol. 16, pp. 5260–5270, 2023, doi: 10.1109/JSTARS.2023.3266794.

[47] X. Xu *et al.*, “An Improved Swin Transformer-Based Model for Remote Sensing Object Detection and Instance Segmentation,” *Remote Sens.*, vol. 13, no. 23, 2021, doi: 10.3390/rs13234779.

[48] C. Zhang, J. Su, Y. Ju, K.-M. Lam, and Q. Wang, “Efficient Inductive Vision Transformer for Oriented Object Detection in Remote Sensing Imagery,” *IEEE Trans. Geosci. Remote Sens.*, vol. 61, pp. 1–20, 2023, doi: 10.1109/TGRS.2023.3292418.

[49] M. Li, J. Lan, Y. Zhang, and K. Huang, “LAST-Net: Local Adaptivity Spatial Transformer Network for Multiobject Detection in UAV Remote Sensing Thermal Infrared Imagery,” *IEEE Trans. Geosci. Remote Sens.*, vol. 63, pp. 1–14, 2025, doi: 10.1109/TGRS.2025.3562966.

[50] W. Lu *et al.*, “A CNN-Transformer Hybrid Model Based on CSWin Transformer for UAV Image Object Detection,” *IEEE J. Sel. Top. Appl. Earth Obs. Remote Sens.*, vol. 16, pp. 1211–1231, 2023, doi: 10.1109/JSTARS.2023.3234161.

[51] C. Zhang, K.-M. Lam, T. Liu, Y.-L. Chan, and Q. Wang, “Structured Adversarial Self-Supervised Learning for Robust Object Detection in Remote Sensing Images,” *IEEE Trans. Geosci. Remote Sens.*, vol. 62, pp. 1–20, 2024, doi: 10.1109/TGRS.2024.3375398.

[52] Y. Zheng, P. Sun, Z. Zhou, W. Xu, and Q. Ren, “ADT-Det: Adaptive Dynamic Refined Single-Stage Transformer Detector for Arbitrary-Oriented Object Detection in Satellite Optical Imagery,” *Remote Sens.*, vol. 13, no. 13, 2021, doi: 10.3390/rs13132623.

[53] M. Yuan and X. Wei, “C²Former: Calibrated and Complementary Transformer for RGB-Infrared Object Detection,” *IEEE Trans. Geosci. Remote Sens.*, vol. 62, pp. 1–12, 2024, doi: 10.1109/TGRS.2024.3376819.

[54] A. Radford *et al.*, “Learning Transferable Visual Models From Natural Language Supervision,” in *Proceedings of the 38th International Conference on Machine Learning*, M. Meila and T. Zhang, Eds., in *Proceedings of Machine Learning Research*, vol. 139. PMLR, Jul. 2021, pp. 8748–8763. [Online]. Available: <https://proceedings.mlr.press/v139/radford21a.html>

[55] F. Yu *et al.*, “ERNIE-ViL: Knowledge Enhanced Vision-Language Representations through Scene Graphs,” *Proc. AAAI Conf. Artif. Intell.*, vol. 35, no. 4, pp. 3208–3216, May 2021, doi: 10.1609/aaai.v35i4.16431.

[56] M. M. A. Rahhal, Y. Bazi, N. A. Alsharif, L. Bashmal, N. Alajlan, and F. Melgani, “Multilanguage Transformer for Improved Text to Remote Sensing Image Retrieval,” *IEEE J. Sel. Top. Appl. Earth Obs. Remote Sens.*, vol. 15, pp. 9115–9126, 2022, doi: 10.1109/JSTARS.2022.3215803.

[57] Z. Zhu, J. Kang, W. Diao, Y. Feng, J. Li, and J. Ni, “SIRS: Multitask Joint Learning for Remote Sensing Foreground-Entity Image–Text Retrieval,” *IEEE Trans. Geosci. Remote Sens.*, vol. 62, pp. 1–15, 2024, doi: 10.1109/TGRS.2024.3402216.

[58] R. Yang *et al.*, “Transcending Fusion: A Multiscale Alignment Method for Remote Sensing Image–Text Retrieval,” *IEEE Trans. Geosci. Remote Sens.*, vol. 62, pp. 1–17, 2024, doi: 10.1109/TGRS.2024.3496898.

[59] J. Yang, S. Li, and M. Zhao, “Parameter-Efficient Reparameterization Tuning for Remote Sensing Image–Text Retrieval,” *IEEE Trans. Geosci. Remote Sens.*, vol. 63, pp. 1–15, 2025, doi: 10.1109/TGRS.2025.3558246.

[60] Y. Wang, X. Tang, J. Ma, X. Zhang, F. Liu, and L. Jiao, “Cross-Modal Remote Sensing Image–Text Retrieval via Context and Uncertainty-Aware Prompt,” *IEEE Trans. Neural Netw. Learn. Syst.*, vol. 36, no. 6, pp. 11384–11398, 2025, doi: 10.1109/TNNLS.2024.3458898.

[61] X. Chen, X. Zheng, and X. Lu, “Context-Aware Local–Global Semantic Alignment for Remote Sensing Image–Text Retrieval,” *IEEE Trans. Geosci. Remote Sens.*, vol. 63, pp. 1–12, 2025, doi: 10.1109/TGRS.2025.3552304.

[62] J. Guan, Y. Shu, W. Li, Z. Song, and Y. Zhang, “PR-CLIP: Cross-Modal Positional Reconstruction for Remote Sensing Image–Text Retrieval,” *Remote Sens.*, vol. 17, no. 13, 2025, doi: 10.3390/rs17132117.

[63] F. Liu *et al.*, “RemoteCLIP: A Vision Language Foundation Model for Remote Sensing,” *IEEE Trans. Geosci. Remote Sens.*, vol. 62, pp. 1–16, 2024, doi: 10.1109/TGRS.2024.3390838.

[64] Z. Zhang, T. Zhao, Y. Guo, and J. Yin, “RS5M and GeoRSCLIP: A Large-Scale Vision- Language Dataset and a Large Vision-Language Model for Remote Sensing,” *IEEE Trans. Geosci. Remote Sens.*, vol. 62, pp. 1–23, 2024, doi: 10.1109/TGRS.2024.3449154.

[65] Z. Wang, R. Prabha, T. Huang, J. Wu, and R. Rajagopal, “SkyScript: A Large and Semantically Diverse Vision-Language Dataset for Remote Sensing,” *Proc. AAAI Conf. Artif. Intell.*, vol. 38, no. 6, pp. 5805–5813, Mar. 2024, doi: 10.1609/aaai.v38i6.28393.

[66] Z. Fu, H. Yan, and K. Ding, “CLIP-MoA: Visual–Language Models With Mixture of Adapters for Multitask Remote Sensing Image Classification,” *IEEE Trans. Geosci. Remote Sens.*, vol. 63, pp. 1–17, 2025, doi: 10.1109/TGRS.2025.3565552.

[67] W. Zhang, M. Cai, T. Zhang, Y. Zhuang, and X. Mao, “EarthGPT: A Universal Multimodal Large Language

> REPLACE THIS LINE WITH YOUR MANUSCRIPT ID NUMBER (DOUBLE-CLICK HERE TO EDIT) <

Model for Multisensor Image Comprehension in Remote Sensing Domain,” *IEEE Trans. Geosci. Remote Sens.*, vol. 62, pp. 1–20, 2024, doi: 10.1109/TGRS.2024.3409624.

[68] J.-B. Alayrac *et al.*, “Flamingo: a Visual Language Model for Few-Shot Learning,” in *Advances in Neural Information Processing Systems*, S. Koyejo, S. Mohamed, A. Agarwal, D. Belgrave, K. Cho, and A. Oh, Eds., Curran Associates, Inc., 2022, pp. 23716–23736. [Online]. Available: https://proceedings.neurips.cc/paper_files/paper/2022/file/960a172bc7fbf0177ccccbb411a7d800-Paper-Conference.pdf

[69] J. Li, D. Li, C. Xiong, and S. Hoi, “BLIP: Bootstrapping Language-Image Pre-training for Unified Vision-Language Understanding and Generation,” in *Proceedings of the 39th International Conference on Machine Learning*, K. Chaudhuri, S. Jegelka, L. Song, C. Szepesvari, G. Niu, and S. Sabato, Eds., in *Proceedings of Machine Learning Research*, vol. 162. PMLR, Jul. 2022, pp. 12888–12900. [Online]. Available: <https://proceedings.mlr.press/v162/li22n.html>

[70] K. Li, Z. Wu, K.-C. Peng, J. Ernst, and Y. Fu, “Tell Me Where to Look: Guided Attention Inference Network,” in *Proceedings of the IEEE Conference on Computer Vision and Pattern Recognition (CVPR)*, Jun. 2018.

[71] J. Mun, M. Cho, and B. Han, “Text-Guided Attention Model for Image Captioning,” *Proc. AAAI Conf. Artif. Intell.*, vol. 31, no. 1, Feb. 2017, doi: 10.1609/aaai.v31i1.11237.

[72] S. Petryk, L. Dunlap, K. Nasser, J. Gonzalez, T. Darrell, and A. Rohrbach, “On Guiding Visual Attention With Language Specification,” in *Proceedings of the IEEE/CVF Conference on Computer Vision and Pattern Recognition (CVPR)*, Jun. 2022, pp. 18092–18102.

[73] G. Ang and E.-P. Lim, “Guided Attention Multimodal Multitask Financial Forecasting with Inter-Company Relationships and Global and Local News,” in *Proceedings of the 60th Annual Meeting of the Association for Computational Linguistics (Volume 1: Long Papers)*, S. Muresan, P. Nakov, and A. Villavicencio, Eds., Dublin, Ireland: Association for Computational Linguistics, May 2022, pp. 6313–6326. doi: 10.18653/v1/2022.acl-long.437.

[74] L. Yu, H. Zhang, and C. Xu, “Text-Guided Attention is All You Need for Zero-Shot Robustness in Vision-Language Models,” in *Advances in Neural Information Processing Systems*, A. Globerson, L. Mackey, D. Belgrave, A. Fan, U. Paquet, J. Tomczak, and C. Zhang, Eds., Curran Associates, Inc., 2024, pp. 96424–96448. doi: 10.52202/079017-3056.

[75] S. Srivastava and H. Sharma, “Deep Multimodal Relational Reasoning and Guided Attention for Chart Question Answering,” *J. Electron. Imaging*, vol. 33, no. 6, p. 063052, 2024, doi: 10.1117/1.JEI.33.6.063052.

[76] L. Tosato, H. Boussaid, F. Weissgerber, C. Kurtz, L. Wendling, and S. Lobry, “Segmentation-Guided Attention for Visual Question Answering from Remote Sensing Images,” in *IGARSS 2024 - 2024 IEEE International Geoscience and Remote Sensing Symposium*, 2024, pp. 2750–2754. doi: 10.1109/IGARSS53475.2024.10642082.

[77] S. Wang, Q. Hu, S. Wang, P. Zhao, J. Li, and M. Ai, “Category Attention Guided Network for Semantic Segmentation of Fine-Resolution Remote Sensing Images,” *Int. J. Appl. Earth Obs. Geoinformation*, vol. 127, p. 103661, 2024, doi: <https://doi.org/10.1016/j.jag.2024.103661>.

[78] B. Zhu *et al.*, “Gradient Structure Information-Guided Attention Generative Adversarial Networks for Remote Sensing Image Generation,” *Remote Sens.*, vol. 15, no. 11, 2023, doi: 10.3390/rs15112827.

[79] A. Larsen *et al.*, “A Deep Learning Approach to Identify Smoke Plumes in Satellite Imagery in Near-Real Time for Health Risk Communication,” *J. Expo. Sci. Environ. Epidemiol.*, vol. 31, no. 1, pp. 170–176, Jan. 2021, doi: 10.1038/s41370-020-0246-y.

[80] H. S. Cunha *et al.*, “Water tank and swimming pool detection based on remote sensing and deep learning: Relationship with socioeconomic level and applications in dengue control,” *PLOS ONE*, vol. 16, no. 12, pp. 1–24, Dec. 2021, doi: 10.1371/journal.pone.0258681.

[81] J.-B. Xue *et al.*, “Recognizing and monitoring infectious sources of schistosomiasis by developing deep learning models with high-resolution remote sensing images,” *Infect. Dis. Poverty*, vol. 12, no. 1, p. 6, Feb. 2023, doi: 10.1186/s40249-023-01060-9.

[82] H. W. Chen, C.-Y. Chen, K. L. P. Nguyen, B.-J. Chen, and C.-H. Tsai, “Hyperspectral sensing of heavy metals in soil by integrating AI and UAV technology,” *Environ. Monit. Assess.*, vol. 194, no. 7, p. 518, Jun. 2022, doi: 10.1007/s10661-022-10125-5.

[83] M. Wang *et al.*, “Pollution level mapping of heavy metal in soil for ground-airborne hyperspectral data with support vector machine and deep neural network: A case study of Southwestern Xiong'an, China,” *Environ. Pollut.*, vol. 321, p. 121132, 2023, doi: <https://doi.org/10.1016/j.envpol.2023.121132>.

[84] E. Suel, S. Bhatt, M. Brauer, S. Flaxman, and M. Ezzati, “Multimodal deep learning from satellite and street-level imagery for measuring income, overcrowding, and environmental deprivation in urban areas,” *Remote Sens. Environ.*, vol. 257, p. 112339, 2021, doi: <https://doi.org/10.1016/j.rse.2021.112339>.

[85] Y. Zhang, N. Chen, W. Du, Y. Li, and X. Zheng, “Multi-source sensor based urban habitat and resident health sensing: A case study of Wuhan, China,” *Build. Environ.*, vol. 198, p. 107883, 2021, doi: <https://doi.org/10.1016/j.buildenv.2021.107883>.

[86] A. Maharana and E. O. Nsoesie, “Use of Deep Learning to Examine the Association of the Built Environment With Prevalence of Neighborhood Adult Obesity,” *JAMA Netw. Open*, vol. 1, no. 4, pp. e181535–e181535, Aug. 2018, doi: 10.1001/jamanetworkopen.2018.1535.

[87] J.-E. Bibault, M. Bassenne, H. Ren, and L. Xing, “Deep Learning Prediction of Cancer Prevalence from Satellite

> REPLACE THIS LINE WITH YOUR MANUSCRIPT ID NUMBER (DOUBLE-CLICK HERE TO EDIT) <

Imagery,” *Cancers*, vol. 12, no. 12, 2020, doi: 10.3390/cancers12123844.

[88] A. Deonarine, G. Lyons, C. Lakhani, and W. De Brouwer, “Identifying Communities at Risk for COVID-19-Related Burden Across 500 US Cities and Within New York City: Unsupervised Learning of the Coprevalence of Health Indicators,” *JMIR Public Health Surveill*, vol. 7, no. 8, p. e26604, Aug. 2021, doi: 10.2196/26604.

[89] D. Pala *et al.*, “Deep Learning to Unveil Correlations between Urban Landscape and Population Health,” *Sensors*, vol. 20, no. 7, 2020, doi: 10.3390/s20072105.

[90] J. J. Levy, R. M. Lebeaux, A. G. Hoen, B. C. Christensen, L. J. Vaickus, and T. A. MacKenzie, “Using Satellite Images and Deep Learning to Identify Associations Between County-Level Mortality and Residential Neighborhood Features Proximal to Schools: A Cross-Sectional Study,” *Front. Public Health*, vol. 9, 2021, doi: 10.3389/fpubh.2021.766707.

[91] Centers for Disease Control and Prevention, “PLACES: Local Data for Better Health.” 2021. [Online]. Available: <https://www.cdc.gov/places/index.html>

[92] D. Aaronson, D. Hartley, and B. Mazumder, “The Effects of the 1930s HOLC ‘Redlining’ Maps,” *Am. Econ. J. Econ. Policy*, vol. 13, no. 4, pp. 355–92, Nov. 2021, doi: 10.1257/pol.20190414.

[93] R. K. Nelson, L. Winling, R. Marciano, N. Connolly, and E. L. Ayers, “Mapping Inequality: Redlining in New Deal America.” 2023.

[94] Census Bureau, “American Community Survey.” 2022. [Online]. Available: <https://www.census.gov/programs-surveys/acs.html>

[95] X. Qi *et al.*, “MLRSNet: A multi-label high spatial resolution remote sensing dataset for semantic scene understanding,” *ISPRS J. Photogramm. Remote Sens.*, vol. 169, pp. 337–350, 2020, doi: <https://doi.org/10.1016/j.isprsjprs.2020.09.020>.

[96] Mistral AI, “Mistral AI Model.” [Online]. Available: <https://huggingface.co/mistralai/Mistral-7B-Instruct-v0.3>

[97] Z. Liu *et al.*, “Swin Transformer V2: Scaling Up Capacity and Resolution,” in *2022 IEEE/CVF Conference on Computer Vision and Pattern Recognition (CVPR)*, 2022, pp. 11999–12009. doi: 10.1109/CVPR52688.2022.01170.

[98] H. Bao, L. Dong, S. Piao, and F. Wei, “BEiT: BERT Pre-Training of Image Transformers.” 2022. [Online]. Available: <https://arxiv.org/abs/2106.08254>

[99] W. Wang *et al.*, “PVT v2: Improved baselines with pyramid vision transformer,” *Comput. Vis. Media*, vol. 8, no. 3, pp. 415–424, 2022, doi: 10.1007/s41095-022-0274-8.

Supplemental Document for

Observing Health Outcomes Using Remote Sensing Imagery and Geo-Context Guided Visual Transformer

Yu Li, *Member, IEEE*, Guilherme N. DeSouza, *Senior Member, IEEE*, Praveen Rao, *Senior Member, IEEE*, Chi-Ren Shyu, *Senior Member, IEEE*

SUPPLEMENTAL TABLE I
DETAILED PERFORMANCE OF GCGVT-A WITH LIMITED GEOSPATIAL INFORMATION

Category	Arthritis		Cancer		CHD		COPD		Depression		Diabetes		Kidney		Obesity		Stroke	
	I+G	G	I+G	G	I+G	G	I+G	G	I+G	G	I+G	G	I+G	G	I+G	Geo	I+G	G
Age	0.72	0.40	0.81	0.76	0.62	0.42	0.58	0.26	0.65	0.09	0.59	0.32	0.53	0.27	0.71	0.41	0.53	0.30
Ancestry	0.52	0.21	0.47	0.30	0.43	0.28	0.58	0.38	0.68	0.39	0.72	0.59	0.53	0.38	0.82	0.57	0.61	0.41
Education	0.58	0.35	0.48	0.44	0.51	0.37	0.68	0.51	0.65	0.19	0.67	0.54	0.55	0.41	0.79	0.68	0.56	0.43
Employment	0.67	0.38	0.54	0.35	0.68	0.54	0.75	0.60	0.66	0.15	0.76	0.65	0.68	0.65	0.75	0.59	0.72	0.65
Household	0.69	0.43	0.73	0.68	0.60	0.54	0.64	0.43	0.67	0.26	0.71	0.58	0.66	0.60	0.79	0.59	0.68	0.64
Housing	0.71	0.66	0.58	0.59	0.67	0.63	0.74	0.71	0.68	0.36	0.74	0.65	0.70	0.66	0.71	0.72	0.73	0.66
Income	0.75	0.64	0.72	0.62	0.71	0.68	0.77	0.70	0.68	0.32	0.77	0.73	0.75	0.76	0.81	0.73	0.77	0.76
Origin	0.52	0.28	0.27	0.22	0.36	0.28	0.52	0.32	0.62	0.20	0.55	0.38	0.39	0.27	0.66	0.46	0.43	0.30
Race	0.57	0.40	0.45	0.37	0.42	0.27	0.54	0.34	0.67	0.14	0.76	0.65	0.57	0.48	0.83	0.64	0.64	0.54
Residency	0.51	0.03	0.37	0.19	0.35	0.01	0.49	<0	0.62	<0	0.46	<0	0.33	0.04	0.59	0.19	0.40	<0
All	0.84	0.81	0.86	0.88	0.80	0.79	0.83	0.82	0.85	0.76	0.88	0.86	0.84	0.83	0.90	0.87	0.85	0.84
Diff	0.24±0.11		0.09±0.07		0.13±0.09		0.21±0.12		0.45±0.10		0.16±0.11		0.12±0.09		0.19±0.11		0.14±0.11	

Note: Column I+G in each outcome is using both image and geospatial information, and G is using only geospatial embedding. Row Diff shows mean plus-minus standard deviation of difference between I+G and G across categories, not including row All.

SUPPLEMENTAL TABLE II
TOP 3 PERFORMANCE OF GCGVT-A WITH IMAGE AND TWO GEOSPATIAL CATEGORY COMBINATIONS

Outcome	Image with Categories	R ²	Difference
Arthritis	AgeSex+Housing	0.83	0.02
	AgeSex+Income	0.81	0.00
	AgeSex+Employment	0.80	-0.01
Cancer	AgeSex+Ancestry	0.85	-0.03
	AgeSex+Education	0.84	-0.04
	AgeSex+Race	0.84	-0.04
CHD	AgeSex+Income	0.79	0.00
	AgeSex+Housing	0.79	0.00
	AgeSex+Employment	0.77	-0.02
COPD	Employment+Income	0.81	0.00
	AgeSex+Income	0.80	-0.02
	AgeSex+Housing	0.80	-0.02
Depression	Ancestry+Income	0.78	0.02
	Income+Race	0.78	0.02
	Ancestry+Housing	0.77	0.01
Diabetes	Income+Race	0.86	0.00
	Housing+Race	0.84	-0.02
	Ancestry+Housing	0.84	-0.02
Kidney	AgeSex+Income	0.79	-0.04
	AgeSex+Housing	0.78	-0.05
	Ancestry+Income	0.77	-0.06
Obesity	Income+Race	0.88	0.01
	Education+Race	0.88	0.01
	Ancestry+Education	0.87	0.00
Stroke	Income+Race	0.82	-0.03
	AgeSex+Income	0.80	-0.04
	Housing+Race	0.79	-0.05

SUPPLEMENTAL TABLE III
EXAMPLES OF GENERATED SUMMARY FROM GEOSPATIAL INFORMATION AND CORRESPONDING IMAGE

Image	Generated Summary
	This area predominantly comprises middle-aged to older adults, with a significant share of Hispanic and Asian populations, and a large number of suburban households, where a majority of part-time occupations are observed.
	This area exhibits significant disparities in socioeconomic status, with a majority of households belonging to the lower and very low income categories, and a substantial proportion of the population being African American or Hispanic.
	This area exhibits a predominantly young population, particularly among householders, with a significant share of them being single, female, and elderly, and a notable absence of children. The majority of householders are native, and socioeconomically, they are primarily employed, with a large share working in the service sector.
	This area predominantly consists of a significant number of households belonging to the Asian and White ethnicities, with a substantial minority of Hispanic households, particularly among the younger population. The majority of households are homeowners, and a considerable share of them are middle-aged or older. The employment status is primarily full-time, and the median income is above the national average.
	This area predominantly consists of older households, with a significant minority of young households, and a large share of the population is native-born, particularly of Hispanic, Black, and White ethnicities, with a high proportion of married couples and a considerable number of homeowners.
	This area predominantly consists of young households, with a significant share of renters, particularly among the lower-income population, and a high prevalence of commuting, with a majority of workers employed in the service sector.
	This area predominantly comprises middle-aged to older households, with a significant minority of young adults, and a small share of children. The majority of households are homeowners, and a considerable portion of them are employed in the service sector. The median income is relatively low, and there is a high level of social assistance utilization.
	This area predominantly comprises middle-aged homeowners, with a significant minority of retirees and a smaller share of young adults, particularly those in the labor force. The majority of homes are owned, and a substantial number are senior-occupied.
	This area is predominantly composed of middle-aged households, with a significant share of married or cohabiting couples, and a large proportion of females heading single-unit dwellings, particularly among older-aged units. The majority of households are homeowners, and a substantial number of them are Hispanic or African American. The most common occupation is in the service industry.